Understanding Structural and Electronic Properties of Bismuth Trihalides and Related Compounds

Zeyu Deng,[†] Fengxia Wei,[‡] Yue Wu,[†] Ram Seshadri,[¶] Anthony K. Cheetham,[†,¶] and Pieremanuele Canepa[*,†]

[†]Department of Materials Science and Engineering, National University of Singapore, 9 Engineering Drive 1, Singapore

[‡]Institute of Materials Research and Engineering, A*STAR, 2 Fusionopolis Way, Innovis, Singapore

[¶]Materials Department and Materials Research Laboratory, University of California Santa Barbara, California 93106, United States

E-mail: pcanepa@nus.edu.sg

Abstract

Bismuth trihalides, BiX_3 (X=F, Cl, Br and I) have been thrust into prominence recently due to their close chemical relationship to the halide perovskites of lead, which exhibit remarkable performance as active layers in photovoltaic cells and other optoelectronic devices. In the present work we have used calculations based on density functional theory to explore the energetics and electronic properties of BiX_3 in a variety of known and hypothetical structure types. The results for BiX_3 are compared with those obtained for the halides of the later rare-earths, represented by YX_3 and LuX_3. The relative thermodynamic stabilities of the known and hypothetical structures are calculated, along with their band gaps. For the BiX_3 systems we have explored the role of

1

lone pair effects associated with Bi(III), and for BiI_3 we have compared the predicted structural behaviour as a function of pressure with the available experimental data. We have also attempted to synthesize LuF_3 in the perovskite-related ReO_3-type structure, which is predicted to be only ~ 7.7 kJ mol^{-1} above the convex hull. This attempt was unsuccessful, but lead to the discovery of a new hydrated phase, $(H_3O)Lu_3F_{10}H_2O$, which is isomorphous with the known ytterbium analogue.

Introduction

Metal-halide materials possess a rich variety of interesting properties that has resulted in a number of technologically important applications, including their use as scintillator materials for X-rays detection,[1] ionic conductors for energy storage applications,[2,3] and their adoption as photoluminescent materials for bioimaging through up-conversion.[4,5] Recently, hybrid perovskite halides of general formula $A^IPb^{II}X_3$ (A = an amine cation, such as $CH_3NH_3^+$ or $CH(NH_2)_2^+$ and X = Cl, Br and I) have attracted significant interest in relation to photovoltaic (PV) and photoluminescence (PL) applications due to their excellent optoelectronic properties, facile synthesis and low costs.[6–10] However, the toxicity of Pb and the sensitivity to moisture of these perovskites have stimulated efforts to find alternative materials that can provide similar or even superior optoelectronic properties without the toxicity and stability issues. One strategy involves replacing the divalent metal (Pb^{2+}) with a mixture of monovalent M^I and trivalent M^{III} cations to form halide double perovskites of general formula $A_2^IM^IM^{III}X_6$ (A = alkali metal or amine cation),[11–16] and thus expands the structural diversity of the family of these perovskite materials. Most of the work in this area has focused on the use of bismuth as the M^{III} cation, though there has also been work involving antimony,[17] as well as rare-earth elements for possible optical and magnetic applications.[18] Another strategy is to use the bismuth halides themselves, especially BiI_3, which is attracting attention for photovoltaic (PV) cell applications.[19,20] However, the low dimensionality of the layered structure adopted by BiI_3 leads to a wider band gap ($\sim$1.8 eV)[21] compared

with the lead-containing perovskite iodides, hence it is not ideal for PV applications. One approach to solving this problem would be to identify accessible polymorphs of the bismuth halides that retain a 3-D network architecture and should therefore have narrower band gaps. For example, the most obvious structural candidate would be the ReO_3-type structure,[22,23] which has a perovskite architecture with no cation in the cavity (i.e., MX_3).

In this paper we address the question: can we favorably access bismuth halides in 3D structures, such as the ReO_3-type. It is already known that $M^{III}F_3$ compounds, such as ScF_3 and InF_3, adopt the ReO_3 structure, so this is a reasonable hypothesis. However, BiF_3 and $BiCl_3$ normally adopt 3-D structures related to that of YF_3 and the smaller rare-earth fluorides (Sm-Lu), while $BiBr_3$ and BiI_3 both have layered structures that are also seen for the rare-earth chlorides (Dy-Lu), bromides and iodides (Sm-Lu).[24] We have therefore used a computational approach to map the thermodynamic stability of the binary trihalides, MX_3 with M = Bi, Y and Lu and X = F, Cl, Br and I. This strategy has been applied for several structure types, specifically those of BiI_3 (2-D), YCl_3 (2-D), $PuBr_3$ (2-D), ReO_3 (3-D), YF_3 (3-D) and LaF_3 (3-D). We have carried out calculations using density functional theory (DFT) to determine the thermodynamic properties of each the MX_3 phases in the different structure types. Furthermore, we have performed simulations with hybrid functionals to assess the optoelectronic properties of a subset of relevant materials to identify novel candidates as light-absorbers and scintillators. We have also assessed the role of electron lone pairs on bismuth by comparing the results for the BiX_3 systems with those for the rare-earth analogues, YX_3 and LuX_3.

Our computational analysis suggests that although LuF_3 appears metastable in the ReO_3 prototype, it should be accessible through synthetic strategies. We explored the synthesis of this phase in the laboratory through a solution evaporation method and found a hydrated phase, $(H_3O)Lu_3F_{10} \cdot H_2O$, crystallizing in the space group $Fd\bar{3}m$, which has not been reported previously.

Methodology

To assess the thermodynamics of binary trihalides MX_3 with M = Lu, Y, Bi and X = F, Cl, Br and I using first-principles calculations, we computed the total energies of each compound and calculated the formation energies from their elemental constituents. The formation energies (E_f) were calculated as: $E_f = E(M_yX_{4-y}) - yE(M) - (4-y)E(X)$ (y = 1), where $E(M_yX_{4-y})$, $E(M)$ and $E(X)$ are the DFT total energies for MX_3 compound, M metal and X halides, respectively. $E(X)$ is the DFT total energy of element X in its most stable form. For X = F and Cl, $E(F) = E(F_2(g))/2$ or $E(Cl_2(g))/2$, where $E(F_2(g))$ and $E(Cl_2(g))$ were calculated as isolated F_2 or Cl_2 molecules at the centre of a $15 \times 15 \times 15$ $Å^3$ box. We only focus on total energies neglecting entropy contributions, pV and zero-point energies since these are expected to be almost identical when comparing dense solids with similar structure type.[25] Additional details concerning the effects of entropy and the pV term are discussed in the SI with particular reference to LuF_3 in the YF_3 and ReO_3 structure types.

From the formation energy plots (see an example of the convex hull plot in the Supporting Information), the energies above the convex hull, E^{hull}, were then evaluated as: $E^{hull}(MX_3)$ = $E_f(MX_3)$ - $min[E_f(MX_3)]$, where $min[E_f(MX_3)]$ belongs to the MX_3 compound with the lowest formation energy among all different polymorphs. Figure S1 in the Supporting Information shows an example of how we determine the convex hull of a Bi_mX_n system and related E^{hull} at specific compositions, e.g., BiX_3.

DFT calculations were performed using the projected augmented wave (PAW) potentials[26,27] as implemented in VASP[28,29] with the following electrons treated explicitly: Bi $[6s^26p^3]$, Y $[4s^24p^64d^15s^2]$, Lu $[5s^25p^65d^16s^2]$, F $[2s^22p^5]$, Cl $[3s^23p^5]$, Br $[4p^24p^5]$ and I $[5s^25p^5]$. A kinetic-energy cutoff of 520 eV and a Γ-centered Monkhorst-Pack k-point mesh[30] was automatically generated along each reciprocal vector $\vec{b_i}$ with a number of k-points $N_i = max(1, l \times |\vec{b_i}| + 0.5)$ where l is the k-point line density with $l = 25$. The exchange and correlation energy was evaluated by the generalized gradient approximation (GGA), within the Perdew-Burke-Ernzerhof (PBE) functional.[31] Van der Waals forces were captured by

Grimme's method (i.e., DFT-D3 employing zero-damping).[32] The total energy was considered converged within 1×10^{-5} eV. In all cases, both volume and internal coordinates were optimized until the forces were less than 0.01 eV Å^{-1}. Whenever possible, the symmetry of each prototype structure was preserved in these calculations (see Section Structure Description). For high-pressure calculations, $H = E + PV$ was used instead of E, and all structures were relaxed using the same parameters as stated above.

The band gaps of the halides were computed from the fully optimized structures (i.e., volume, shape and internal coordinates) using the HSE06 hybrid functional[33] with van der Waals corrections. Due to the cost of the hybrid-functional calculations, total energies and geometries were converged within the prescribed tolerances set by the pymatgen library.[34] Spin-orbit coupling (SOC) effects were included by performing a single point energy calculation on the fully relaxed HSE06+D3 structures. The inclusion of SOC has been found necessary[35] to describe accurately the electronic structure of compounds containing heavy elements, such as Bi and Pb. Band gaps were estimated from the total densities of states computed on k-point grids, including the special inequivalent symmetry points of the Brillouin Zone of each polymorph. The electron localization function (ELF)[36] was computed with the PBE functional (on the fully relaxed PBE+D3 geometries) to establish the role of lone-pairs in specific structures.

Results and Discussion

Selection of Prototype Structures

We have considered the six structure types shown in Table 1 and Figure 1, for a total of 72 trihalides materials, known and hypothetical, spanning all combinations of the three metals (Bi, Lu, Y) and the four halogens (i.e., F, Cl, Br and I). In addition, we have examined three other structure types: ZrI_3 and UCl_3, BiF_3 (gananite), whose results are shown in Figure S2 and Table S1. The initial structures for energy minimization and geometry optimization

were taken from the Inorganic Crystal Structure Database (ICSD) unless stated otherwise.

Table 1: Space group, coordination number of the metal site (C.N.) and structural dimensionality of the different structure types considered in this study.

Type	Space Group	C.N.	Dimensionality	Comment	Ref.
BiI_3	$R\bar{3}m$	6	2-D layered	ABCABC stacking	37
YCl_3	$C2/m$	6	2-D layered	ABAB stacking	38
$PuBr_3$	$Ccmm$	8	2-D layered	ABAB stacking	39
ReO_3	$Pm\bar{3}m$	6	3-D	Perovskite type framework	40
YF_3	$Pnma$	9	3-D	3-D Complex structure	41
LaF_3	$P\bar{3}c1$	9	3-D	Tysonite	42

Table 1 provides the geometrical characteristics of each structure type, including the coordination number of the metal and structural dimensionality (2-D layered or 3-D network). Of the three metals studied, bismuth was chosen as a potential replacement of toxic Pb in conventional hybrid-perovskite solar cells, as discussed earlier. Yttrium (0.90 Å) and lutetium (0.86 Å) are smaller in ionic radii than bismuth (1.03 Å) when occupying 6-coordinated sites, and are thus potential candidates to form an ReO_3-type structure. In addition, the electronic configurations of Y^{3+} and Lu^{3+} are closed shell, unlike most of the rare-earth elements, and therefore avoid spin-polarized calculations.

BiI_3 and YCl_3 compounds form very similar layered structures, with the major difference in the different stacking arrangement of the layers (see Figure 1 and Table 1). The $PuBr_3$-type structure is also layered and has the same stacking arrangement as YCl_3 (ABAB), but with a higher coordination number of the metal site (8) than in YCl_3 (6). The $PuBr_3$-type structure was included because a number of rare-earth compounds are known to form with this structure type.[24]

Table 2 compares the performance of our computational methodology in describing the lattice constants of the known MX_3 structures for Bi and Y. More details are given in the Supplementary Information. Almost all of our lattice constants from DFT agree within 2% of the experimental values. Since a number of layered structures are considered (e.g., BiI_3 and YCl_3-types), van der Waals forces are treated explicitly to describe correctly the energetics
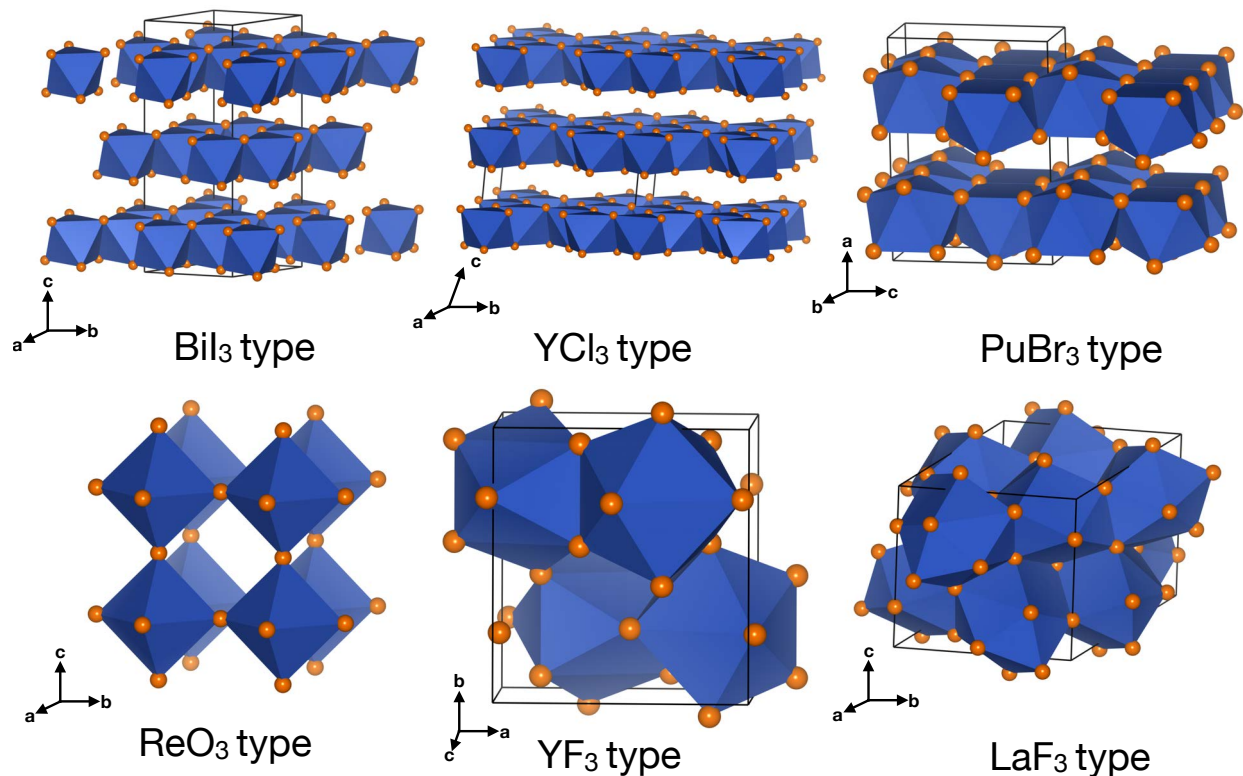
6

Figure 1: The six structural types explored for each system were the BiI_3, YCl_3, $PuBr_3$, ReO_3, YF_3 and LaF_3 structures. The polyhedra show the metal coordination in each structure type.

and thus the structural features.[32] As shown in Table 3, the van der Waals corrections significantly improve the predictions of the lattice parameters and volumes of layered structures such as BiI_3. As expected, the largest improvement is observed for the c lattice parameters, which reflects the layer separation, and the a/c ratio reflects the quality of our simulations against experiment.

Thermodynamic Stability of MX$_3$ Materials

Figure 2a shows the computed volumes (color bar) per formula unit of MX_3 for each compound considered (y-axis) across the six structure types identified (x-axis). The volumes increase systematically from fluoride to iodide-based structures, as well as from Lu^{3+} to Bi^{3+}, due to the increasing ionic radii of these ions. However, there are two exceptions to

7

Table 2: Difference (%) in lattice parameters and unit cell volume between DFT (PBE+D3) calculated values and experiments.

Structure	a	b	c	Ref.
BiF_3	−0.26%	1.10%	1.12%	41
$BiCl_3$	1.08%	−3.67%	1.66%	43
$BiBr_3$	−0.72%	−0.47%	0.67%	44
BiI_3	1.22%	1.22%	1.26%	37
YF_3	0.18%	1.19%	2.18%	41
YCl_3	−0.15%	−0.44%	−0.30%	38
YI_3	0.30%	0.30%	0.72%	45

Table 3: Comparison with experiments of DFT calculated lattice parameters (Å) and unit cell volume for BiI_3 ($Å^3$) for calculations with and without van der Waals corrections. The ratio between a and the lattice constant along the stacking direction is also provided (in brackets: the relative variation to experiment).

	a	c	a/c	V
PBE	7.843 (4.35%)	23.163 (11.79%)	2.953 (7.13%)	1233.91
PBE+D3	7.608 (1.22%)	20.981 (1.26%)	2.758 (0.04%)	1051.67
Exp[37]	7.516	20.720	2.757	1013.66

these trends: for YF_3 in the BiI_3 structure and YI_3 in the $PuBr_3$ type, the volumes are anomalously low. This appears to be caused by the significant distortions that occurred during structure relaxation; for example, YF_3 (in the BiI_3 type) changed dimensionality from an initial 2D to a 3D complex structure, and vice versa for YI_3 (in $PuBr_3$).

The thermodynamic stability for each compound is characterized by its formation energy and its energy above the convex hull (E^{hull}) for different structure types. The color bar of Figure 2b shows the energy above the convex hull (in kJ mol^{-1} per MX_3) for each structure type (x-axis) and compound (y-axis). White areas indicate polymorphs that are not expected to form under any conditions, whereas blue areas show stable structures (dark blue) or potential metastable structures (in lighter shades of blue). Structures identified experimentally are boxed with a white halo. We chose an upper bound of E^{hull} of 20.0 kJ mol^{-1} per MX_3 ($\sim$ 207 meV/MX_3 and $\sim$52.0 meV per atom, respectively) as the threshold between metastable and unstable structures. Sun et al.[46] have recently proposed a threshold for E^{hull} of $\sim$70 meV/atom between metastable and unstable structures, and our upper bound
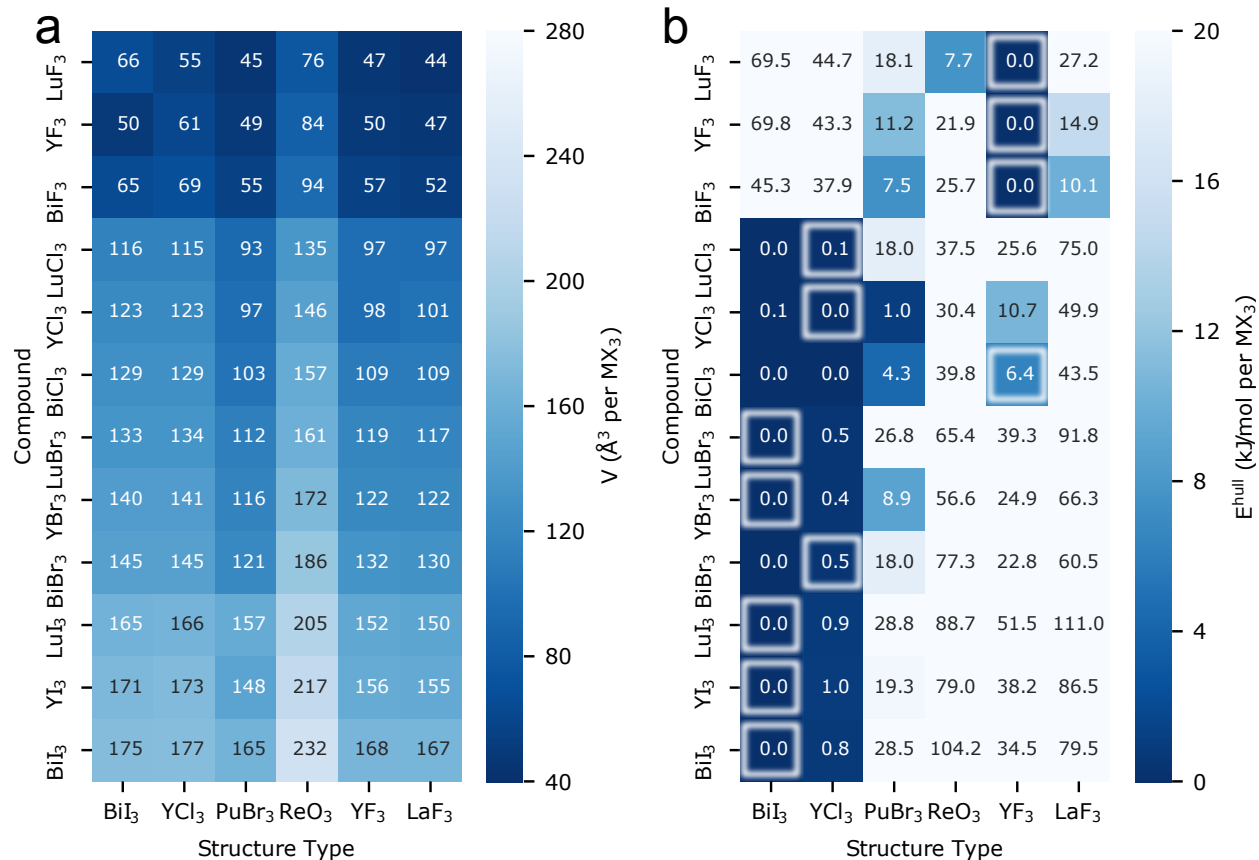
Figure 2: a DFT computed unit cell volumes (V in Å^3 per MX$_3$) per unit formula of MX$_3$, and **b** DFT calculated formation energy above convex hull (E$^{\text{hull}}$ in kJ mol^{-1} per MX$_3$). Experimental identified phases are boxed with white halos.

broadly follows this prescription.

As shown in Figure 2b, the DFT calculations reproduce the correct experimental polymorphs in virtually all cases (see white boxes), with E$^{\text{hull}}$ close to or equal to 0.00 kJ mol^{-1}. Given the structural similarity of the BiI$_3$ type and YCl$_3$ type compounds, values of E$^{\text{hull}}$ for each compound with these two structure types are very similar. The only discrepancy between our DFT prediction and experimental data is found for BiCl$_3$, where DFT suggests a 2D BiI$_3$ (or YCl$_3$)-type structure, whereas a 3D YF$_3$-type structure was reported experimentally.[43] However, the energy of the reported structure is only 6.4 kJ mol^{-1} above the convex hull and the DFT calculation for this structure nicely reproduces the molecular nature of the bonding,[43] with three short Bi-Cl bonds and several much longer ones.

In general, as shown in Figures 2a and b, the stability of ReO_3 type compounds decreases when expanding the volume of either M-cation or X-halide or both. We find that LuF_3 has the lowest energy above the hull ($E^{hull} \sim 7.8$ kJ mol^{-1} per f.u.), hence LuF_3 is the best candidate for adopting the ReO_3 type.

In addition to LuF_3 in the ReO_3 prototype, we have identified other stable or metastable structures, including YCl_3, $BiCl_3$, BiF_3, YBr_3, YF_3, $BiBr_3$, and LuF_3 in the $PuBr_3$ type, and BiF_3 and YF_3 in the LaF_3 type. The $PuBr_3$ structure has both a high coordination number (8) on the metal site and is 2D layered, which is placed between YCl_3/BiI_3 type (low coordination number and dimensionality) and LaF_3/YF_3 type (high coordination number and dimensionality). Therefore, most of these predicted compounds in the $PuBr_3$ structure are close to the convex hull.

In Figure 2b, other general trends can be identified and serve to rationalize the relative stabilities of the these MX_3 polymorphs. For example, we observe that Lu-based compounds in the BiI_3-type strongly prefer the larger anions, Cl$^-$, Br$^-$ and I$^-$, as demonstrated by their low energies above the hull.

It is also important to verify the relative distortions of compounds investigated in this study in comparison to their prototypical structures, e.g., ReO_3, BiI_3 and LaF_3. To this end, we utilize a structure matching algorithm,[47] which computes the minimized root mean square distances. This is defined as $d_{RMS} = \sqrt[3]{n/V_{avg}}\sqrt{(\Sigma_{i=1}^n d_i^2)/n}$ between each compound and a reference structure, where d_i is the Cartesian distances of ith site between two structures, n is the total number of sites, and V_{avg} is the volume of the average lattice of the two structures compared. Our reference structures are the prototypical experimental structures; for example, if we consider LuF_3 in the ReO_3-type, its reference structure would be set by the atomic arrangement in ReO_3 ($Pm\bar{3}m$). Thus, a value of $d_{RMS} = 0$ means that the compound arranged with the structure of its prototype, and hence without any distortion. In contrast, large values of d_{RMS} suggest large distortions after relaxation.

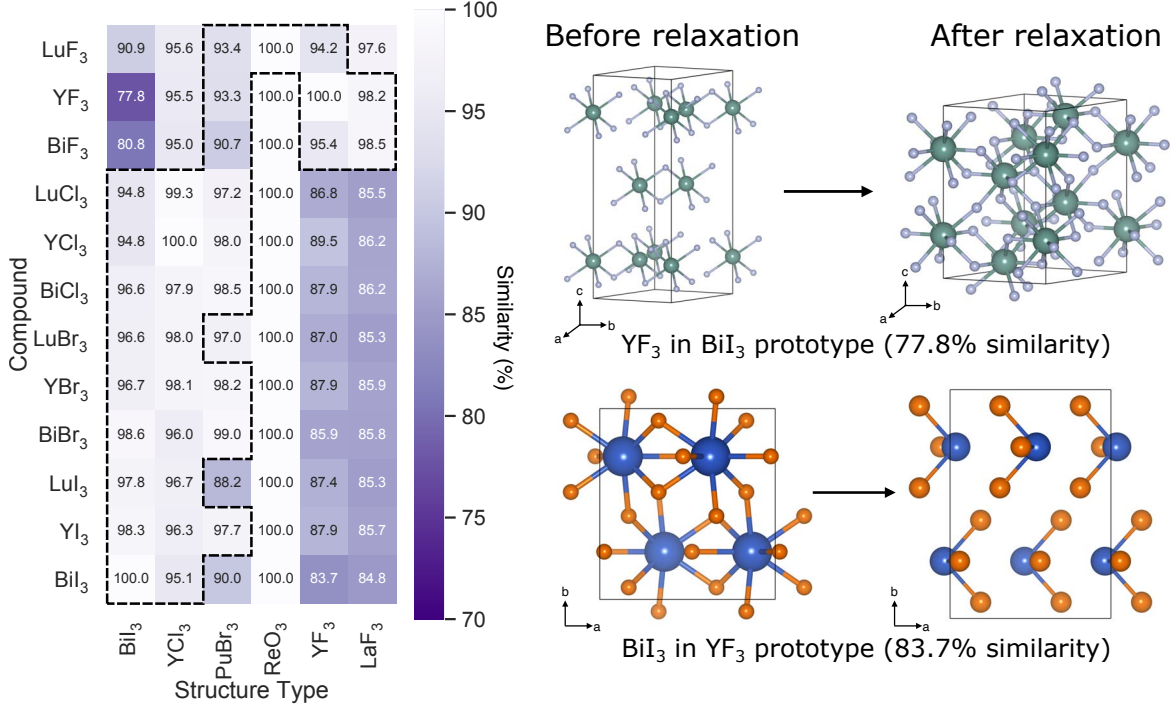Figure 3 shows the relative changes in % (of d_{RMS}), here termed similarity, between

Figure 3: Structural similarity (%) between relaxed compound and their prototypes based on the minimized d_{RMS} computed for each compound and a reference prototype. The dashed black lines are guides for the eye and map the stable or metastable structures identified in Figure 2b. Two examples: YF₃ in the BiI₃ type and BiI₃ in the YF₃ type are shown here.

different compounds and their structure prototypes of origin, where dark purple represents large distortion from the prototype structure of reference. Note that 100% similarity matches with $d_{RMS} = 0$ and 0 % stands for $d_{RMS} = 1$. All compounds with the ReO_3 type structure have 100% similarity due to the symmetry constraint imposed during the relaxation process.

By relating trends of similarity (or d_{RMS}) and thermodynamic stability (Figure 2b), a number of observations can be made. (i) At first glance one can draw an unidirectional link between structures with high thermodynamic stability (i.e., $E^{hull} \sim 0$ kJ per f.u.) and structures with high similarity near 100% (or close to $d_{RMS} = 0$). For example, most chloride, bromide and iodide compounds in the BiI_3/YCl_3 types are thermodynamically stable (Figure 2b), and hence show appreciable similarity with their prototypes, i.e., small distortions after relaxation. Exceptions to this trend are YCl_3 and $BiCl_3$ in the YF_3 type. In particular, YCl_3 forms a layered-type structure, whereas $BiCl_3$ forms an almost isolated

11

molecular-structure, most likely due to the lone pair of Bi^{3+} (as discussed in the next section). (ii) Interestingly, one observes that when fluorine compounds, such as LaF_3 and YF_3, are anion exchanged with the larger halides Cl^-, Br^- or I^-, low values of similarity (i.e., large d_{RMS} values) and low thermodynamic stabilities (Figure 2b) are found. From a closer inspection of the structures of these compounds, we observed their transformation from a 3D compact structure to layered-type structures. Similarly, a transformation implying a change of dimensionality from 2D to 3D can be observed when iodine is exchanged with fluorine, as in the compounds in the top-left side of Figure 3. (iii) Another observation is that high values of similarity, equivalent to low values of d_{RMS}, cannot guarantee low or zero E^{hull}. While most compounds in the ReO_3 type structure are thermodynamically unstable (except for LuF_3), they appear less distorted after relaxation, which we link to the constraint of symmetry and the size of the unit cell adopted.

The Role of the Lone Pair in BiX$_3$ structures

We move now to the analysis of the electronic structure of the known experimental structure types (see Table 1, beginning with a consideration of lone pair effects in the Bi(III) compounds. It is well established that a wide range of Pb(II) and Bi(III) compounds exhibit stereochemically active s^2 lone pairs in systems ranging from inorganic[48] and hybrid perovskites[49] to metal-organic frameworks,[50,51] so it is expected that these effects might be seen in the bismuth halides. We explore this behaviour in the BiX$_3$ phases by analysing the electron localization function (ELF), which enables us to localize the electron lone pairs around Bi(III) (Figure 4). For comparison, we also show the ELF functions for the corresponding Y(III) phases, where no lone pair effect is expected.

In ELF calculations, values near 0.5 are indicative of delocalization of charge similar to a homogeneous electron gas, whereas ELF = 1 suggests areas matching high electron localization. From Figure 4, both BiF_3 and $BiCl_3$ show large ELF values ($\sim$0.8) near the Bi^{3+} cations and the shape of the domain appears highly anisotropic, suggesting significant
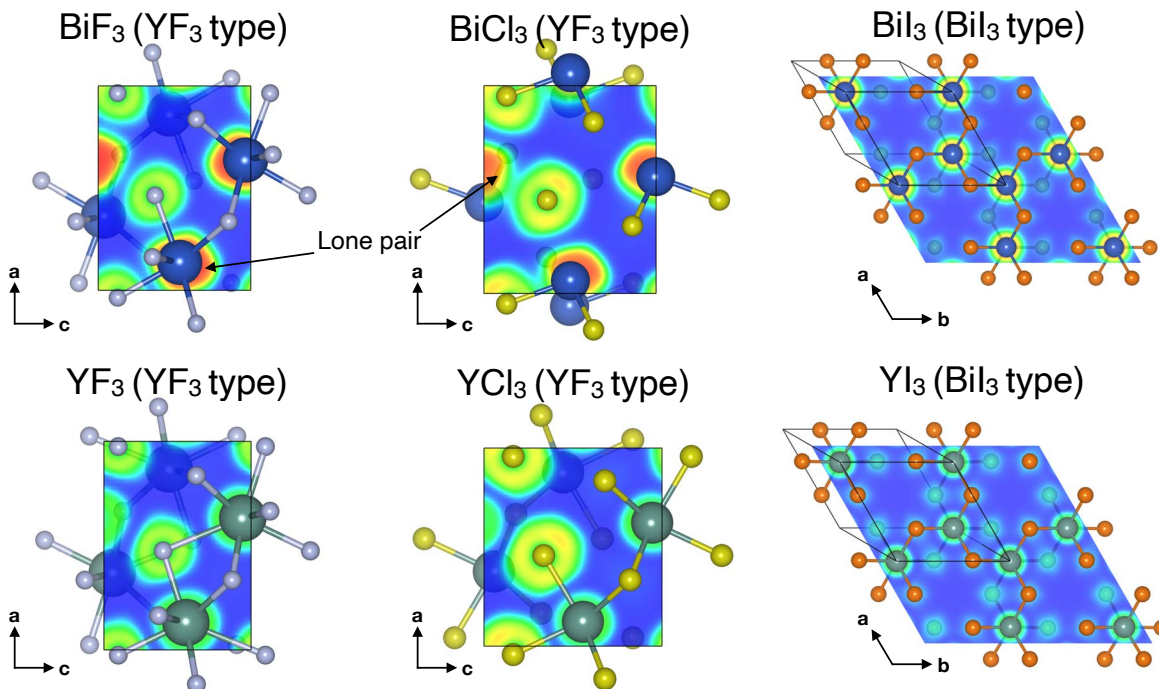
Figure 4: Computed ELFs for BiF$_3$, BiCl$_3$, BiI$_3$, YF$_3$, YCl$_3$ and YI$_3$ in the structure-type shown in brackets. Note that BiBr$_3$ and YBr$_3$ are very similar to the iodide analogues. Colour mapping of the ELF value is shown from 0 (blue) to 1 (red).

localization of the lone pair. The presence of lone pair effects can directly affect the symmetry and unit cell dimensions of crystal structures.[48] For example, in BiF$_3$ the lone pair causes an elongation of the c-axis, increasing the c/a ratio to 0.75;[41] this can be compared with a value of 0.71 in YF$_3$, where the lone pair is not present. In BiCl$_3$, which is virtually molecular, one can observe the arrangement of pyramidal BiCl$_3$ moieties that are held together by van der Waals forces, much as one would find in the structure of ammonia. Because of the distortion imparted by the highly localized lone pair, the overall dimensionality and the coordination number of Bi^{3+} are reduced. This may lead to the confinement of electrons, which is partly responsible for the large band gaps in BiCl$_3$ and BiF$_3$ (see Figure 5). However, in the case of BiBr$_3$ and BiI$_3$ (Figure 4), the lone pairs are not active and the ELFs are very similar to those of the yttrium structures. The tendency of lone pair effects to be stronger with more electronegative ions has been seen in other systems, such as the PbO layered structure

13

(driven by the lone-pair on Pb) compared with the cubic rocksalt structure in PbS, PbSe and PbTe.[52] To some extent, however, the lone pair effect can be influenced by the structure itself, since we note that BiI_3 in a hypothetical YF_3 type structure forms a pyramidal molecular species like that seen experimentally in $BiCl_3$ (see Supplementary Information, Figure S5).
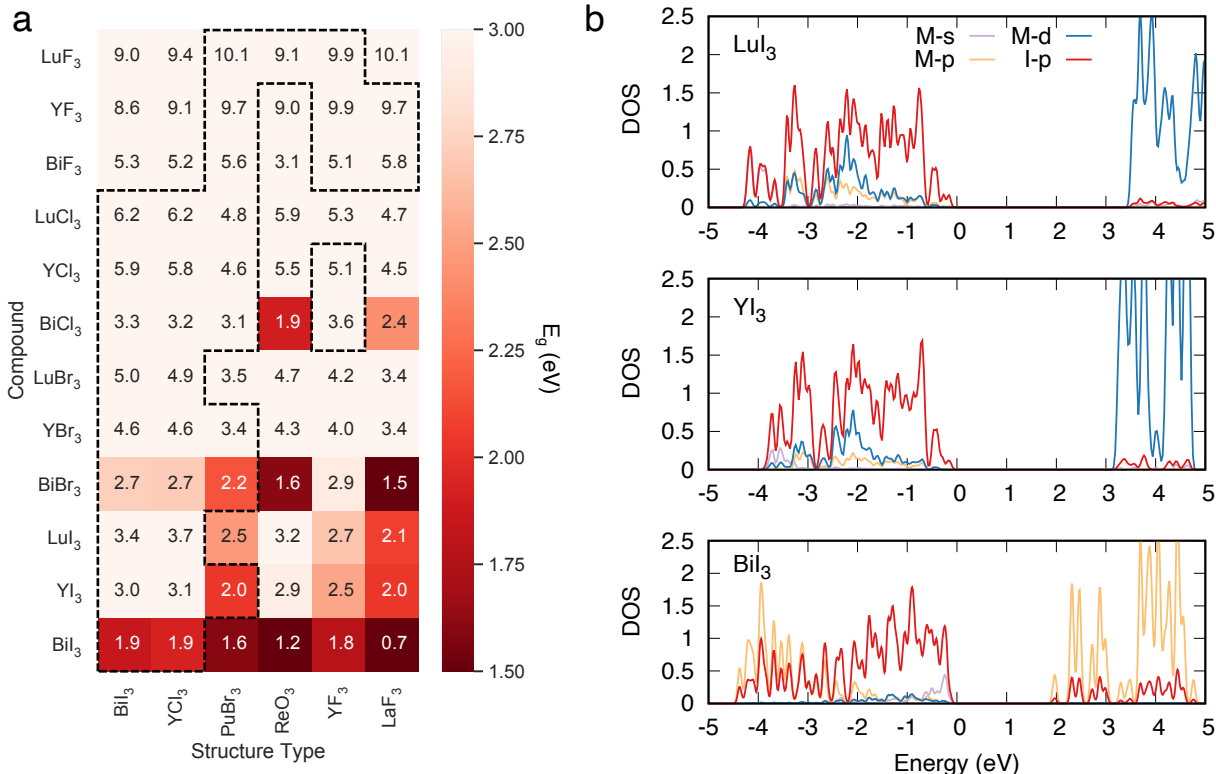
Band Gap Characteristics of MX$_3$

Figure 5: **a Computed energy band gaps (E_g in eV) at the HSE06+D3+SOC level of theory. The dash black lines are guide for mapping the stable or metastable structures identified in Figure 2b. b Projected density of states (pDOS) on selected atomic orbitals of MI$_3$ (M = Lu, Y and Bi) in BiI$_3$ structure type.**

We now move our attention to the opto-electronic properties of the MX$_3$-based materials. Figure 5a shows the band gaps (E_g) computed with the HSE06 hybrid functional, while Table 4 compares our predictions with existing experimental measurements of E_g. When the predicted values of the band-gap are benchmarked against the experimentally reported values in Table 4, we observe that our data with the HSE06 hybrid functional is more accurate.

As in hybrid-perovskite materials, the quantitative description of E_g requires both a higher level of theory (e.g., hybrid functionals or many-body treatments, such as GW) together with spin-orbit coupling corrections.[53]

Table 4: Comparison of E_g (eV) between experiment and DFT calculated values (same structure type).

Compound	$E_{g,DFT}$	$E_{g,Exp}$
YF_3	9.9	10.30[54]
$BiCl_3$	3.6	3.37[55]
$BiBr_3$	2.7	2.66[55]
BiI_3	1.9	1.67,[56] 1.8[19,21]

The E_g in halides decreases moving down the halogen group, i.e., from F^- to I^-, as expected. For example, in Bi-containing compounds (experimental structure type) the band gap decreases systematically as BiF_3 (5.1 eV) > $BiCl_3$ (3.6 eV) > $BiBr_3$ (2.7 eV) > BiI_3 (1.9 eV). As for the metal site, Bi-based compounds show always the lowest band gaps compared to Y- and Lu-based compounds, with Y materials showing slightly lower band gaps than Lu compounds.

We complement this analysis with the projected density of states (pDOS) on specific atomic orbitals of selected structures to identify the orbital character of both valence and conduction bands. As an example, the pDOS of LuI_3, YI_3 and BiI_3 in the BiI_3-type structure are shown in Figure 5b. For valence bands, LuI_3 and YI_3 are dominated by I-$5p$ states, whereas in BiI_3, Bi-$6s$ also contributes significantly to the density of states. The conduction bands of LuI_3 and YI_3 are mostly dominated by Y-$3d$ and Lu-$4d$ with small contributions from I-$5p$ levels, whereas the BiI_3 conduction band is dominated mostly by Bi-$6p$ and I-$5p$ states. Therefore, the Bi-$6s$ and Bi-$6p$ states in the band edges result in a much smaller band gap for BiI_3 compared with YI_3 and LuI_3. As aforementioned for the halide species, the larger the ionic radius of the metal, the lower the band gap.[57]

It is often observed that band-gaps in materials decrease under external pressure; for example, in hybrid halide perovskites, high pressure compression can induce a redshift of photoluminescence (PL) energy.[58] Having explored a number of BiX_3 phases in different
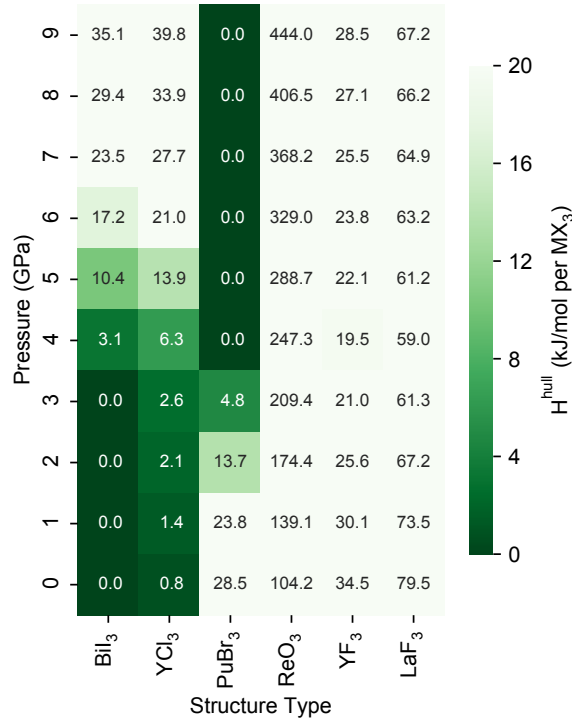
Figure 6: DFT calculated formation enthalpy above convex hull (H^{hull} in kJ mol^{-1} per MX$_3$) of BiI$_3$ composition in different structure types upon pressure.

structures (e.g., BiI$_3$ in the PuBr$_3$ structure), we can now explain some of the observations that have been made in various high-pressure studies of BiI$_3$. Experimentally, Darnell et al.[59] suggested that there is a phase transition of BiI$_3$ at ~2.5 GPa, while Hsueh et al.[60] showed a phase transition from a rhombohedral ($R\bar{3}$) structure to a monoclinic ($P2_1/c$) distorted PuBr$_3$-type structure beyond ~7 GPa. In addition, Devidas et al.[61] reported that BiI$_3$ becomes metallic at ~1.5 GPa, and observed another phase transition to a monoclinic ($P2_1/c$) structure at ~8.8 GPa. To elucidate the relative stabilities of different forms of BiI$_3$ at different pressures, we present in Figure 6 the computed formation enthalpies above the convex hull H^{hull} from ambient pressure up to 9 GPa. Figure 6 shows that below 3 GPa, the 6-coordinated layered BiI$_3$-type is the most stable structure for BiI$_3$, as observed experimentally. At a pressure of ~3-4 GPa, we predict a phase transition from the BiI$_3$ type to a monoclinic distorted from the higher coordinated PuBr$_3$ type, and it remains stable for

pressures up to 9 GPa, which is also in agreement with experiments.[60,62] Note that the 3-D YF$_3$ and LaF$_3$ types are not expected to be stable at any pressure. We have also performed DFT calculations on the experimental distorted PuBr$_3$-type structure that Hsueh et al.[60] reported at different pressures, and the results are similar to our PuBr$_3$-type (see Figure S6) in the high pressure (> 2 GPa) region, although it transformed back to the layered 6-coordinated YCl$_3$-type in the low pressure ($0-2$ GPa) region. Our lattice constants for the PuBr$_3$ form of BiI$_3$ at 8 GPa are in agreement with synchrotron X-ray data collected at $\sim$7.31 GPa by Hsueh et al.[60] (see Table S2 in the SI). The band gap of this high-pressure phase at 8 GPa was calculated (HSE06+D3+SOC) and found to be significantly lower ($\sim$1.0 eV) that of the layered BiI$_3$-type ($\sim$1.6 eV) at ambient pressure.
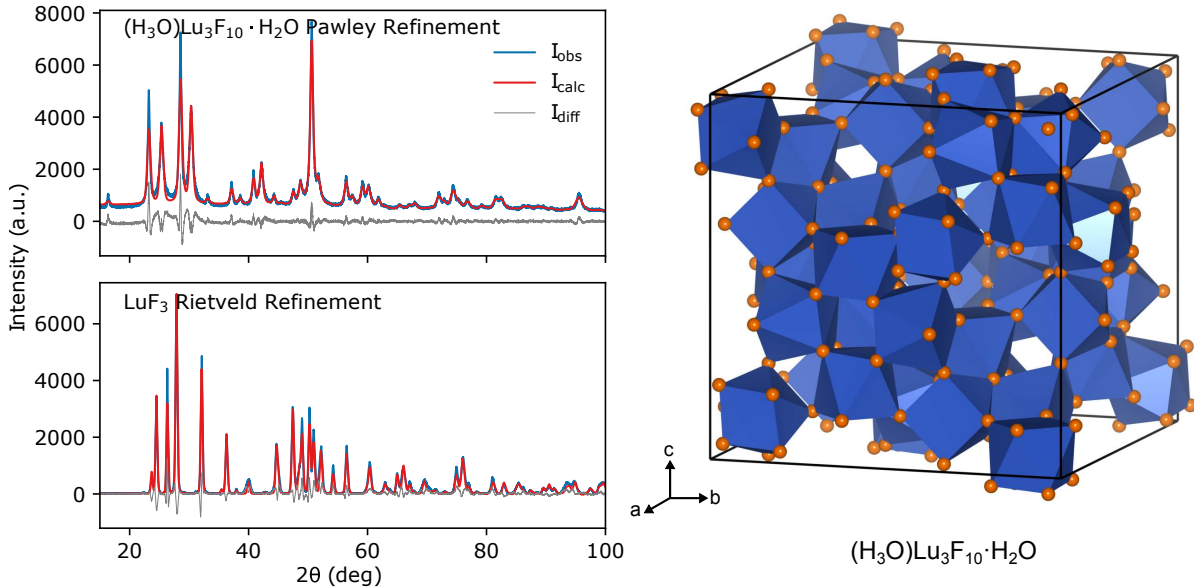

Figure 7: Left: Pawley refinement (top) for the white precipitates of (H$_3$O)Lu$_3$F$_{10}$·H$_2$O with space group $Fd\bar{3}m$**,** $a = $ **15.2967(5)Å; Rietveld refinement (bottom) of LuF$_3$ in** $Pnma$ **with** $a = $ **6.1149(3) Å,** $b = $ **6.7595(3) Å and** $c = $ **4.5064(3) Å. Right: Crystal structure of (H$_3$O)Lu$_3$F$_{10}$·H$_2$O (H$_2$O molecules are not shown).**

Experimental attempts to make the ReO_3 form of LuF_3

Based on our DFT calculations (Figure 2b), LuF_3 has the lowest E^{hull} with the ReO_3 type structure, so it is expected to be the best candidate for adopting that structure. Zalkin and Templeton[62] reported a mixture of unresolved phases in their solution preparation of LuF_3, which further encouraged us to explore this idea. They also observed that heating their initial reaction product lead to the formation of the orthorhombic YF_3-type structure. Experimental attempts to synthesis LuF_3 have therefore been carried out. Following their recipe, 15 mg of Lu_2O_3 was fully dissolved in 5 ml of concentrated HCl acid at 50 °C, and the solution was then neutralized by NH_4OH solution. A few drops of concentrated HF acid (47 wt% in H_2O) was added into the solution to obtain a white precipitate. The mixture was centrifuged, washed by DI water and then dried in air. Zalkin and Templeton were unable to solve the complicate pattern, but we have found that it is a complex acid hydrate, $(H_3O)Lu_3F_{10}·H_2O$, and is isomorphous with $(H_3O)Yb_3F_{10}·H_2O$[63] (see Figure 7, right). $(H_3O)Lu_3F_{10}·H_2O$ has cubic symmetry, space group $Fd\bar{3}m$ with $a = 15.2967(5)$ Å. Structure solution was carried out using TOPAS Academic 6.0 and a Pawley refinement is shown in Figure 7, top left (details on the structure determination and associated crystallographic information are reported in the SI). After heating the powder at 100 °C for 1 hour, an orthorhombic phase with the YF_3-type structure was obtained, as described by Zalkin and Templeton[62] (PXRD result is shown in Figure 7, left bottom). Other synthetic methods, e.g., the thermal evaporation until dryness at 90 °C or hydrothermal synthesis using $Lu(NO_3)_3$ or Lu_2O_3 and diluted HF acid at 120 °C, also give the orthorhombic YF_3 type structure. We have found no evidence for the formation of the ReO_3 modification of LuF_3.

Conclusions

In this study, systematic first-principles calculations have been used to map the chemical space of BiX_3 halides and the analogous MX_3 compositions with M = Y and Lu. Cal-

culations for 12 different MX_3 compositions, each with 9 potential polymorphs, reveal the thermodynamic stabilities of MX_3 in different structure types. The results for the thermodynamically stable phases are in very good agreement with experiment. The qualitative trends follow the radius ratios of the cation M and anion X (r_M/r_X) such that the coordination number of the cations increases as the anion size decreases. For example, the smallest anion, F^-, strongly favors the highly coordinated environment that is found in the YF_3 structure, whereas larger anions, especially I^-, prefer a 6-coordinated cation environment and form YCl_3 or BiI_3 structures.

It is also found that the dimensionality of the crystal structures of MX_3 is strongly correlated to the size of the anion. For compositions with large anions, such as Br^- and I^-, a lower dimensional structure is favoured, e.g., BiI_3 (2D), YCl_3 (2D). $PuBr_3$ (2D), ZrI_3 (1D) and AlI_3 (0D, molecular dimer). The reason for this is that the cation-anion packing density plays an important role in determining its dimensionality and a higher cation-anion packing density is favoured energetically. From Figure 2a, it is shown that, with the same coordination number of 6, the unit cell volumes of the high dimensional ReO_3 type structures are much higher than the corresponding layered BiI_3/YCl_3 types in the case of large anion (Br^- and I^-). Van der Waals interactions also provide additional stabilization in denser structures, and not only to the layered ones. We note that, even without considering van der Waals forces explicitly in our calculations, the layered BiI_3/YCl_3 types remain the most stable structures for large anions (see Figure S4). This observation shows that layered structures are not solely stabilized by van der Waals forces. However, when van der Waals forces are not included in the calculations, the ReO_3 structure is predicted to be favoured relative to the YF_3 type for LuF_3 (Figure S4). In this case, the observed structure is clearly stabilised by the van der Waals forces.

Taken together, these considerations confirm that in order to form a three dimensional 6-coordinated ReO_3 type structure, small anions, e.g., F^-, together with small cations such as Al^{3+}, Sc^{3+} or smaller transitional metal cations, are required. LuF_3 follows this trend, though

our experimental synthesis also showed that even LuF_3 cannot form an ReO_3 type framework. We find that other candidates with desirable properties for photovoltaic applications, such as BiI_3 in the ReO_3-type structure, are not energetically accessible due to their low packing densities. Even under pressure, it is not possible to stabilize the BiI_3 with the ReO_3 structure since the denser $PuBr_3$ type becomes more stable.

The important role of electron localization as lone pairs in the BiX_3 compounds has been seen in the cases of both BiF_3 and $BiCl_3$, both in terms of their structures and their band gaps. Though it is widely believed that stereochemically active lone pairs are particularly prevalent in systems containing more electronegative anions, e.g., fluoride, chloride and oxide, we also find that even BiI_3 would be distorted if it was to adopt a YF_3 type structure. It would appear that the ability of different structure-types to accommodate distortions is more important than was hitherto believed in determining the sensitivity to lone pair effects.

Acknowledgement

Supporting Information Available

The Supporting Information contains: i) Figure S1 shows the convex hulls of BiX (with X=F, Cl, Br and I). ii) Table S1 reports details of other structure types also considered in this study. iii) Table S2 reports the effects of pressure on a number of structure types. iv) Figures S3 and S4 the computed formation energies and volumes using the PBE and PBE+D3 functionals, respectively. v) Figure S5 the ELF plots of selected structures. vi) Figure S6 reports the

formation enthalpies of the BiI_3 composition in different structure types. *vii*) Table S3 shows details on the effects of Entropy and pV terms on the thermodynamic stability of different structure types. *viii*) A final section on the experimental method and the determination of the newly synthesized $(H_3O)Lu_3F_{10}\cdot H_2O$ structure.

References

(1) Blasse, G. Scintillator materials. *Chem. Mater.* **1994**, *6*, 1465–1475, DOI: `10.1021/cm00045a002`.

(2) Cui, X.; Hu, T.; Wang, J.; Zhang, J.; Zhong, X.; Chen, Y.; Li, X.; Yang, J.; Gao, C. Ionic Transportation and Dielectric Properties of YF_3:Eu^{3+} Nanocrystals. *Nanomaterials* **2018**, *8*, 995, DOI: `10.3390/nano8120995`.

(3) Trnovcová, V.; Garashina, L.; Škubla, A.; Fedorov, P.; Čička, R.; Krivandina, E.; Sobolev, B. Structural aspects of fast ionic conductivity of rare earth fluorides. *Solid State Ion.* **2003**, *157*, 195–201, DOI: `10.1016/S0167-2738(02)00209-6`.

(4) Wang, F.; Liu, X. Recent advances in the chemistry of lanthanide-doped upconversion nanocrystals. *Chem. Soc. Rev.* **2009**, *38*, 976, DOI: `10.1039/b809132n`.

(5) Yan, R. X.; Li, Y. D. Down/Up Conversion in Ln^{3+}-Doped YF_3 Nanocrystals. *Adv. Funct. Mater.* **2005**, *15*, 763–770, DOI: `10.1002/adfm.200305044`.

(6) Kojima, A.; Teshima, K.; Shirai, Y.; Miyasaka, T. Organometal Halide Perovskites as Visible-Light Sensitizers for Photovoltaic Cells. *J. Am. Chem. Soc.* **2009**, *131*, 6050–6051, DOI: `10.1021/ja809598r`.

(7) Lee, M. M.; Teuscher, J.; Miyasaka, T.; Murakami, T. N.; Snaith, H. J. Efficient Hybrid Solar Cells Based on Meso-Superstructured Organometal Halide Perovskites. *Science* **2012**, *338*, 643–647, DOI: `10.1126/science.1228604`.

(8) Snaith, H. J. Perovskites: The Emergence of a New Era for Low-Cost, High-Efficiency Solar Cells. *J. Phys. Chem. Lett.* **2013**, *4*, 3623–3630, DOI: `10.1021/jz4020162`.

(9) Protesescu, L.; Yakunin, S.; Bodnarchuk, M. I.; Krieg, F.; Caputo, R.; Hendon, C. H.; Yang, R. X.; Walsh, A.; Kovalenko, M. V. Nanocrystals of Cesium Lead Halide Perovskites ($CsPbX_3$, X = Cl, Br, and I): Novel Optoelectronic Materials Showing Bright Emission with Wide Color Gamut. *Nano Lett.* **2015**, *15*, 3692–3696, DOI: `10.1021/nl5048779`.

(10) Kasel, T. W.; Deng, Z.; Mroz, A. M.; Hendon, C. H.; Butler, K. T.; Canepa, P. Metal-free perovskites for non linear optical materials. *Chem. Sci.* **2019**, *10*, 8187–8194, DOI: `10.1039/c9sc03378e`.

(11) Morss, L. R.; Siegal, M.; Stenger, L.; Edelstein, N. Preparation of cubic chloro complex compounds of trivalent metals: Cs_2NaMCl_6. *Inorg. Chem.* **1970**, *9*, 1771–1775, DOI: `10.1021/ic50089a034`.

(12) Slavney, A. H.; Hu, T.; Lindenberg, A. M.; Karunadasa, H. I. A Bismuth-Halide Double Perovskite with Long Carrier Recombination Lifetime for Photovoltaic Applications. *J. Am. Chem. Soc.* **2016**, *138*, 2138–2141, DOI: `10.1021/jacs.5b13294`.

(13) McClure, E. T.; Ball, M. R.; Windl, W.; Woodward, P. M. Cs_2AgBiX_6 (X = Br, Cl): New Visible Light Absorbing, Lead-Free Halide Perovskite Semiconductors. *Chem. Mater.* **2016**, *28*, 1348–1354, DOI: `10.1021/acs.chemmater.5b04231`.

(14) Volonakis, G.; Filip, M. R.; Haghighirad, A. A.; Sakai, N.; Wenger, B.; Snaith, H. J.; Giustino, F. Lead-Free Halide Double Perovskites via Heterovalent Substitution of Noble Metals. *J. Phys. Chem. Lett.* **2016**, *7*, 1254–1259, DOI: `10.1021/acs.jpclett.6b00376`.

(15) Wei, F.; Deng, Z.; Sun, S.; Xie, F.; Kieslich, G.; Evans, D. M.; Carpenter, M. A.; Bristowe, P. D.; Cheetham, A. K. The synthesis, structure and electronic properties of a

lead-free hybrid inorganic–organic double perovskite $(MA)_2KBiCl_6$ (MA = methylammonium). *Mater. Horiz.* **2016**, *3*, 328–332, DOI: `10.1039/c6mh00053c`.

(16) Deng, Z.; Wei, F.; Sun, S.; Kieslich, G.; Cheetham, A. K.; Bristowe, P. D. Exploring the properties of lead-free hybrid double perovskites using a combined computational-experimental approach. *J. Mater. Chem. A* **2016**, *4*, 12025–12029, DOI: `10.1039/c6ta05817e`.

(17) Wei, F.; Deng, Z.; Sun, S.; Hartono, N. T. P.; Seng, H. L.; Buonassisi, T.; Bristowe, P. D.; Cheetham, A. K. Enhanced visible light absorption for lead-free double perovskite $Cs_2AgSbBr_6$. *Chem. Commun.* **2019**, *55*, 3721–3724, DOI: `10.1039/c9cc01134j`.

(18) Deng, Z.; Wei, F.; Brivio, F.; Wu, Y.; Sun, S.; Bristowe, P. D.; Cheetham, A. K. Synthesis and Characterization of the Rare-Earth Hybrid Double Perovskites: $(CH_3NH_3)_2KGdCl_6$ and $(CH_3NH_3)_2KYCl_6$. *J. Phys. Chem. Lett.* **2017**, *8*, 5015–5020, DOI: `10.1021/acs.jpclett.7b02322`.

(19) Lehner, A. J.; Wang, H.; Fabini, D. H.; Liman, C. D.; Hébert, C.-A.; Perry, E. E.; Wang, M.; Bazan, G. C.; Chabinyc, M. L.; Seshadri, R. Electronic structure and photovoltaic application of BiI_3. *Appl. Phys. Lett.* **2015**, *107*, 131109, DOI: `10.1063/1.4932129`.

(20) Hamdeh, U. H.; Nelson, R. D.; Ryan, B. J.; Bhattacharjee, U.; Petrich, J. W.; Panthani, M. G. Solution-Processed BiI_3 Thin Films for Photovoltaic Applications: Improved Carrier Collection via Solvent Annealing. *Chem. Mater.* **2016**, *28*, 6567–6574, DOI: `10.1021/acs.chemmater.6b02347`.

(21) Brandt, R. E.; Kurchin, R. C.; Hoye, R. L. Z.; Poindexter, J. R.; Wilson, M. W. B.; Sulekar, S.; Lenahan, F.; Yen, P. X. T.; Stevanović, V.; Nino, J. C.; Bawendi, M. G.;

Buonassisi, T. Investigation of Bismuth Triiodide (BiI$_3$) for Photovoltaic Applications. *J. Phys. Chem. Lett.* **2015**, *6*, 4297–4302, DOI: `10.1021/acs.jpclett.5b02022`.

(22) Evans, H. A.; Deng, Z.; Collings, I. E.; Wu, Y.; Andrews, J. L.; Pilar, K.; Tuffnell, J. M.; Wu, G.; Wang, J.; Dutton, S. E.; Bristowe, P. D.; Seshadri, R.; Cheetham, A. K. Polymorphism in M(H$_2$PO$_2$)$_3$ (M = V, Al, Ga) compounds with the perovskite-related ReO$_3$ structure. *Chem. Commun.* **2019**, *55*, 2964–2967, DOI: `10.1039/c9cc00118b`.

(23) Evans, H. A.; Wu, Y.; Seshadri, R.; Cheetham, A. K. Perovskite-related ReO$_3$-type structures. *Nat. Rev. Mater.* **2020**, In press.

(24) Wells, A. F. *Structural Inorganic Chemistry*; Oxford University Press, 2012.

(25) van de Walle, A.; Ceder, G. The effect of lattice vibrations on substitutional alloy thermodynamics. *Rev. Mod. Phys.* **2002**, *74*, 11–45, DOI: `10.1103/revmodphys.74.11`.

(26) Kresse, G.; Joubert, D. From ultrasoft pseudopotentials to the projector augmented-wave method. *Phys. Rev. B* **1999**, *59*, 1758–1775, DOI: `10.1103/physrevb.59.1758`.

(27) Blöchl, P. E. Projector augmented-wave method. *Phys. Rev. B* **1994**, *50*, 17953–17979, DOI: `10.1103/physrevb.50.17953`.

(28) Kresse, G.; Furthmüller, J. Efficient iterative schemes forab initiototal-energy calculations using a plane-wave basis set. *Phys. Rev. B* **1996**, *54*, 11169–11186, DOI: `10.1103/physrevb.54.11169`.

(29) Kresse, G.; Furthmüller, J. Efficiency of ab-initio total energy calculations for metals and semiconductors using a plane-wave basis set. *Comput. Mater. Sci.* **1996**, *6*, 15–50, DOI: `10.1016/0927-0256(96)00008-0`.

(30) Monkhorst, H. J.; Pack, J. D. Special points for Brillouin-zone integrations. *Phys. Rev. B* **1976**, *13*, 5188–5192, DOI: `10.1103/physrevb.13.5188`.

(31) Perdew, J. P.; Burke, K.; Ernzerhof, M. Generalized Gradient Approximation Made Simple. *Phys. Rev. Lett.* **1996**, *77*, 3865–3868, DOI: `10.1103/physrevlett.77.3865`.

(32) Grimme, S.; Antony, J.; Ehrlich, S.; Krieg, H. A consistent and accurate ab initio parametrization of density functional dispersion correction (DFT-D) for the 94 elements H-Pu. *J. Chem. Phys.* **2010**, *132*, 154104, DOI: `10.1063/1.3382344`.

(33) Krukau, A. V.; Vydrov, O. A.; Izmaylov, A. F.; Scuseria, G. E. Influence of the exchange screening parameter on the performance of screened hybrid functionals. *J. Chem. Phys.* **2006**, *125*, 224106, DOI: `10.1063/1.2404663`.

(34) Ong, S. P.; Richards, W. D.; Jain, A.; Hautier, G.; Kocher, M.; Cholia, S.; Gunter, D.; Chevrier, V. L.; Persson, K. A.; Ceder, G. Python Materials Genomics (pymatgen): A robust, open-source python library for materials analysis. *Comput. Mater. Sci.* **2013**, *68*, 314–319, DOI: `10.1016/j.commatsci.2012.10.028`.

(35) Even, J.; Pedesseau, L.; Jancu, J.-M.; Katan, C. Importance of Spin–Orbit Coupling in Hybrid Organic/Inorganic Perovskites for Photovoltaic Applications. *J. Phys. Chem. Lett.* **2013**, *4*, 2999–3005, DOI: `10.1021/jz401532q`.

(36) Silvi, B.; Savin, A. Classification of chemical bonds based on topological analysis of electron localization functions. *Nature* **1994**, *371*, 683–686, DOI: `10.1038/371683a0`.

(37) Keller, L.; Nason, D. Review of X-ray powder diffraction data of rhombohedral bismuth tri-iodide. *Powder Diffr.* **1996**, *11*, 91–96, DOI: `10.1017/s0885715600009040`.

(38) Templeton, D. H.; Carter, G. F. The Crystal Structures of Yttrium Trichloride and Similar Compounds. *J. Phys. Chem* **1954**, *58*, 940–944, DOI: `10.1021/j150521a002`.

(39) Zachariasen, W. H. Crystal chemical studies of the 5f-series of elements. I. New structure types. *Acta Cryst.* **1948**, *1*, 265–268, DOI: `10.1107/s0365110x48000703`.

(40) Meisel, K. Rheniumtrioxyd. III. Mitteilung. Über die Kristallstruktur des Rheniumtrioxyds. *Z. Anorg. Allg. Chem.* **1932**, *207*, 121–128, DOI: `10.1002/zaac.19322070113`.

(41) Cheetham, A. K.; Norman, N. The Structures of Yttrium and Bismuth Trifluorides by Neutron Diffraction. *Acta Chem. Scand.* **1974**, *28a*, 55–60, DOI: `10.3891/acta.chem.scand.28a-0055`.

(42) Cheetham, A. K.; Fender, B. E. F.; Fuess, H.; Wright, A. F. A powder neutron diffraction study of lanthanum and cerium trifluorides. *Acta Cryst. B* **1976**, *32*, 94–97, DOI: `10.1107/s0567740876002380`.

(43) Nyburg, S. C.; Ozin, G. A.; Szymański, S. T. The crystal and molecular structure of bismuth trichloride. Corrigendum. *Acta Cryst. B* **1972**, *28*, 2885–2885, DOI: `10.1107/s0567740872007113`.

(44) von Benda, H. Zur Polymorphie des Wismuttribromids. *Z. Krist.-Cryst. Mater.* **1980**, *151*, DOI: `10.1524/zkri.1980.151.3-4.271`.

(45) Jongen, L.; Meyer, G. Yttrium triiodide, YI_3. *Acta Crystallographica Section E Structure Reports* **2005**, *61*, i151–i152, DOI: `10.1107/s1600536805019847`.

(46) Sun, W.; Dacek, S. T.; Ong, S. P.; Hautier, G.; Jain, A.; Richards, W. D.; Gamst, A. C.; Persson, K. A.; Ceder, G. The thermodynamic scale of inorganic crystalline metastability. *Sci. Adv.* **2016**, *2*, e1600225, DOI: `10.1126/sciadv.1600225`.

(47) Wang, Y.; Richards, W. D.; Ong, S. P.; Miara, L. J.; Kim, J. C.; Mo, Y.; Ceder, G. Design principles for solid-state lithium superionic conductors. *Nat. Mater.* **2015**, *14*, 1026–1031, DOI: `10.1038/nmat4369`.

(48) Seshadri, R.; Hill, N. A. Visualizing the Role of Bi 6s "Lone Pairs" in the Off-Center Distortion in Ferromagnetic $BiMnO_3$. *Chem. Mater.* **2001**, *13*, 2892–2899, DOI: `10.1021/cm010090m`.

(49) Fabini, D. H.; Siaw, T. A.; Stoumpos, C. C.; Laurita, G.; Olds, D.; Page, K.; Hu, J. G.; Kanatzidis, M. G.; Han, S.; Seshadri, R. Universal Dynamics of Molecular Reorientation in Hybrid Lead Iodide Perovskites. *J. Am. Chem. Soc.* **2017**, *139*, 16875–16884, DOI: 10.1021/jacs.7b09536.

(50) Ayyappan, S.; de Delgado, G. D.; Cheetham, A. K.; Férey, G.; Rao, C. N. R. Synthesis and characterization of a three-dimensional open-framework lead(II) carboxyethylphosphonate, $Pb_3(O_2CCH_2CH_2PO_3)_2$. *J. Chem. Soc., Dalton Trans.* **1999**, 2905–2907, DOI: 10.1039/a905326c.

(51) Thirumurugan, A.; Cheetham, A. K. Anionic Metal-Organic Frameworks of Bismuth Benzenedicarboxylates: Synthesis, Structure and Ligand-Sensitized Photoluminescence. *Eur. J. Inorg. Chem.* **2010**, *2010*, 3823–3828, DOI: 10.1002/ejic.201000535.

(52) Walsh, A.; Payne, D. J.; Egdell, R. G.; Watson, G. W. Stereochemistry of post-transition metal oxides: revision of the classical lone pair model. *Chem. Soc. Rev.* **2011**, *40*, 4455, DOI: 10.1039/c1cs15098g.

(53) Umari, P.; Mosconi, E.; Angelis, F. D. Relativistic GW calculations on $CH_3NH_3PbI_3$ and $CH_3NH_3SnI_3$ Perovskites for Solar Cell Applications. *Sci. Rep.* **2014**, *4*, DOI: 10.1038/srep04467.

(54) Sarantopoulou, E.; Kollia, Z.; Cefalas, A. YF_3: Nd^{3+}, Pr^{3+}, Gd^{3+} wide band gap crystals as optical materials for 157-nm photolithography. *Opt. Mater.* **2001**, *18*, 23–26, DOI: 10.1016/s0925-3467(01)00124-0.

(55) Li, K.; Xu, Z.; Xu, H.; Ryan, J. M. Semiconductive Coordination Networks from 2,3,6,7,10,11-Hexakis(alkylthio)triphenylenes and Bismuth(III) Halides:Âă Synthesis, Structure–Property Relations, and Solution Processing. *Chem. Mater.* **2005**, *17*, 4426–4437, DOI: 10.1021/cm050377+.

(56) Podraza, N. J.; Qiu, W.; Hinojosa, B. B.; Motyka, M. A.; Phillpot, S. R.; Baciak, J. E.; Trolier-McKinstry, S.; Nino, J. C. Band gap and structure of single crystal BiI3: Resolving discrepancies in literature. *J. Appl. Phys.* **2013**, *114*, 033110, DOI: `10.1063/1.4813486`.

(57) Brown, I. D. What factors determine cation coordination numbers? *Acta Cryst. B* **1988**, *44*, 545–553, DOI: `10.1107/s0108768188007712`.

(58) Jaffe, A.; Lin, Y.; Beavers, C. M.; Voss, J.; Mao, W. L.; Karunadasa, H. I. High-Pressure Single-Crystal Structures of 3D Lead-Halide Hybrid Perovskites and Pressure Effects on their Electronic and Optical Properties. *ACS Cent. Sci.* **2016**, *2*, 201–209, DOI: `10.1021/acscentsci.6b00055`.

(59) Darnell, A. J.; McCollum, W. A. Phase diagrams of the bismuth trihalides at high pressure. *J. Phys. Chem.* **1968**, *72*, 1327–1334, DOI: `10.1021/j100850a045`.

(60) Hsueh, H. C.; Chen, R. K.; Vass, H.; Clark, S. J.; Ackland, G. J.; Poon, W. C.-K.; Crain, J. Compression mechanisms in quasimolecular XI_3 (X=As,Sb,Bi) solids. *Phys. Rev. B* **1998**, *58*, 14812–14822, DOI: `10.1103/physrevb.58.14812`.

(61) Devidas, T. R.; Shekar, N. V. C.; Sundar, C. S.; Chithaiah, P.; Sorb, Y. A.; Bhadram, V. S.; Chandrabhas, N.; Pal, K.; Waghmare, U. V.; Rao, C. N. R. Pressure-induced structural changes and insulator-metal transition in layered bismuth triiodide, BiI_3: a combined experimental and theoretical study. *J. Phys.: Condens. Matter* **2014**, *26*, 275502, DOI: `10.1088/0953-8984/26/27/275502`.

(62) Zalkin, A.; Templeton, D. H. The Crystal Structures of YF_3 and Related Compounds. *J. Am. Chem. Soc.* **1953**, *75*, 2453–2458, DOI: `10.1021/ja01106a052`.

(63) Maguer, J.-J.; Crosnier-Lopez, M.; Courbion, G. "Chimie Douce" Synthesis and ab Initio Structure Determination of $(H_3O)Yb_3F_{10}$,H_2O: Diamond Type Stacking of UOA[8]. *J. Solid State Chem.* **1997**, *128*, 42–51, DOI: `10.1006/jssc.1996.7145`.

Graphical TOC Entry
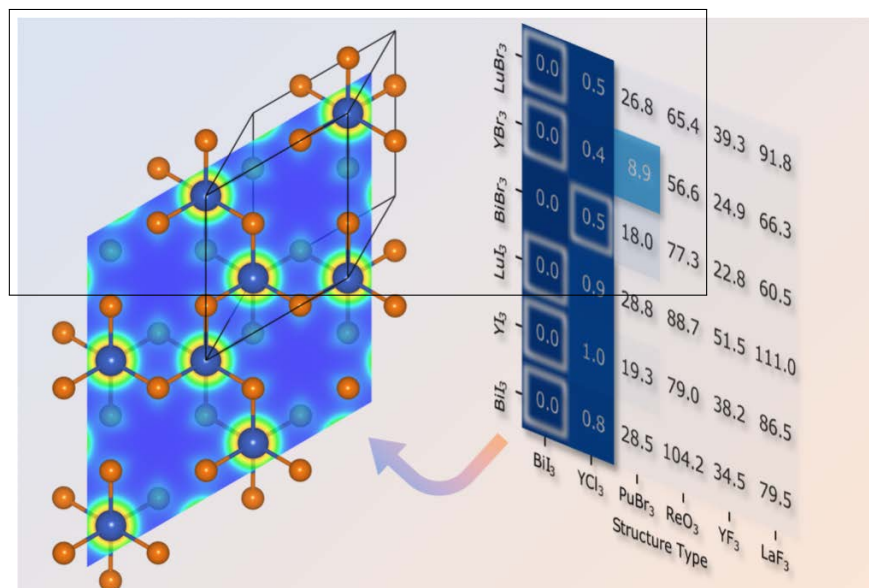
The relative stabilities of bismuth and rare-earth tri-halides are calculated in different structure types and the role of the lone pair on bismuth in determining structure is examined.

—Supporting Information—
Understanding Structural and Electronic Properties of Bismuth Trihalides and Related Compounds

Zeyu Deng,[†] Fengxia Wei,[‡] Yue Wu,[†] Ram Seshadri,[¶] Anthony K. Cheetham,[†,¶] and Pieremanuele Canepa[*,†]

†*Department of Materials Science and Engineering, National University of Singapore, 9 Engineering Drive 1, Singapore*

‡*Institute of Materials Research and Engineering, A*STAR, 2 Fusionopolis Way, Innovis, Singapore*

¶*Materials Department and Materials Research Laboratory, University of California Santa Barbara, California 93106, United States*
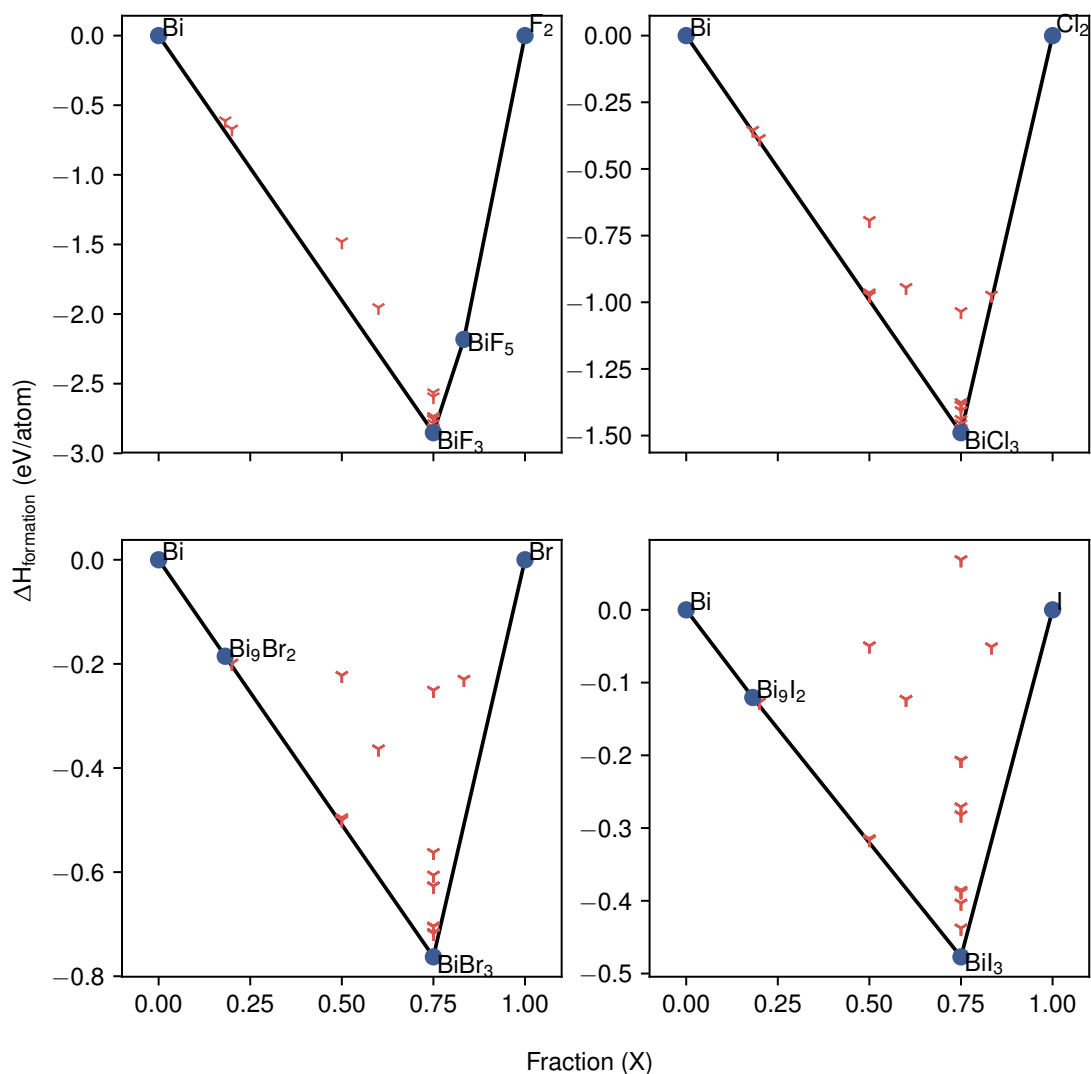
E-mail: pcanepa@nus.edu.sg

Figure S1: DFT calculated phase diagrams (Bi-X) of $Bi_{1-y}X_y$ (X = F, Cl, Br and I, y = 0 ∼ 1) in terms of their formation energies. The stability line, convex hull is plotted using black solid lines. Stable compounds are marked using blue points, whereas unstable phases (above convex hull) are shown by red cross.
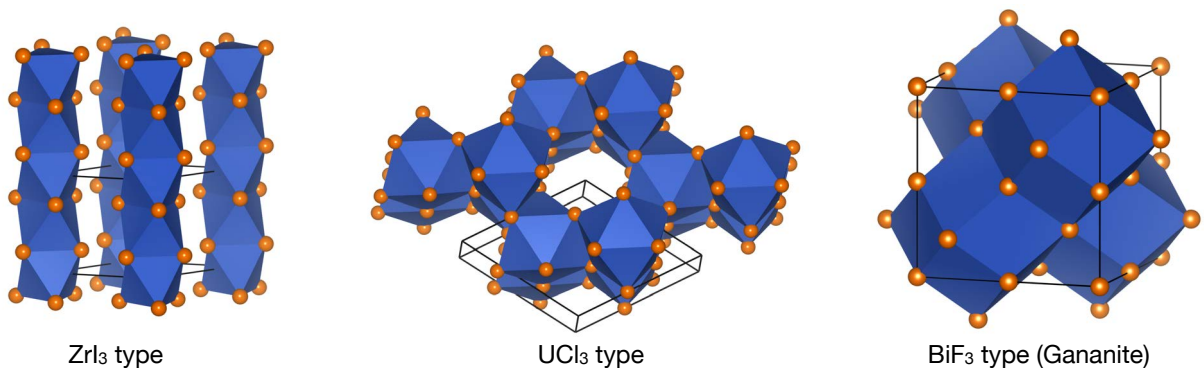
Figure S2: The additional structural types explored for each system were the ZrI₃, UCl₃ and BiF₃ (Gananite) structures. The polyhedra show the metal co-ordination found in each case.

Table S1: Space group, coordination number of the metal site (C.N.) and structural dimensionality of other structure types considered shown in Figure S2.

Type	Space Group	C.N.	Dimensionality	Comment	Ref.
ZrI_3	$P6_3/mcm$	6	1-D	Face sharing 1D chain	1
UCl_3	$P6_3/m$	9	3-D	3D Complex structure	2
BiF_3	$P\bar{4}3m$	10	3-D	Gananite	3

Table S2: Comparison with experiments of DFT calculated lattice parameters (Å) for BiI₃ at 7 and 8 GPa. Note that due to the constrain of the periodic condition of the starting PuBr₃ prototype, our calculated unit cell along c direction is only half the size compared with experimental BiI₃ at 7.31 GPa. So doubled lattice parameters along the c-axis are shown in brackets.

	a	b	c	β
This work, PuBr₃-type[a] (7 GPa)	6.768	9.402	4.117 (8.234)	107.7°
This work, (7 GPa)	6.767	9.398	8.234	107.7°
This work, PuBr₃0type[a] (8 GPa)	6.723	9.352	4.093 (8.185)	107.7°
This work, (8 GPa)	6.720	9.354	8.185	107.7°
Exp., (7.31 GPa)[4]	6.728	9.565	8.106	107.6°

[a]PuBr₃ type structures are based-centered orthorhombic and the lattice parameters of their primitive cells are shown here.
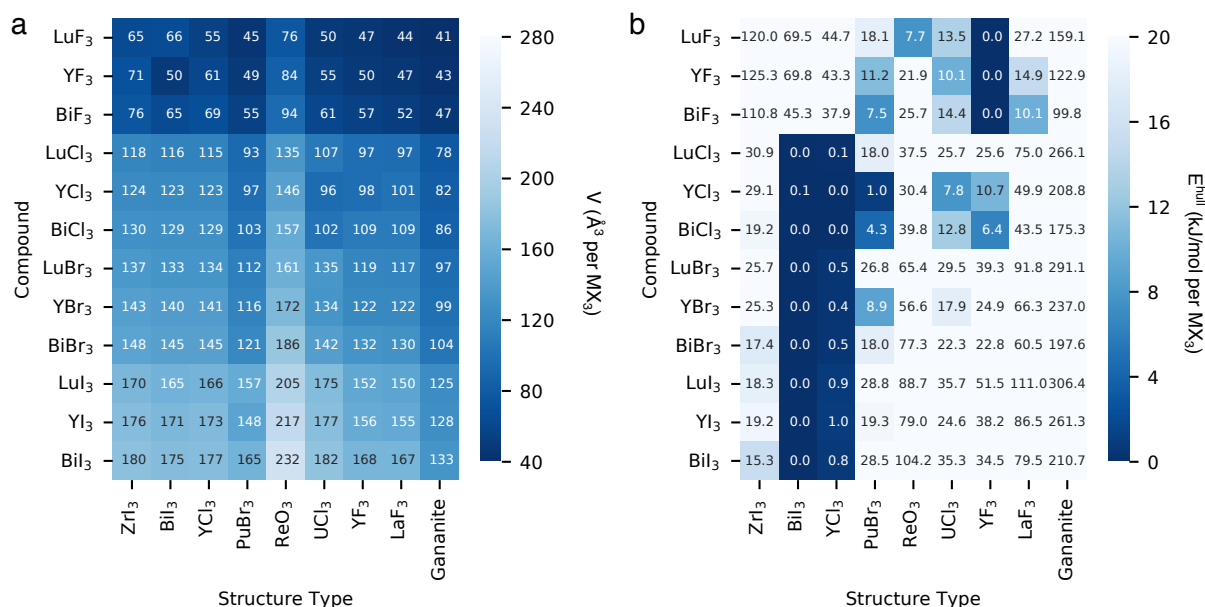
Figure S3: a DFT (PBE+D3) calculated unit cell volumes (V in Å³ per MX₃) per unit formula of MX₃, and **b** DFT calculated formation free energy above convex hull (Eʰᵘˡˡ in kJ mol⁻¹ per MX₃).
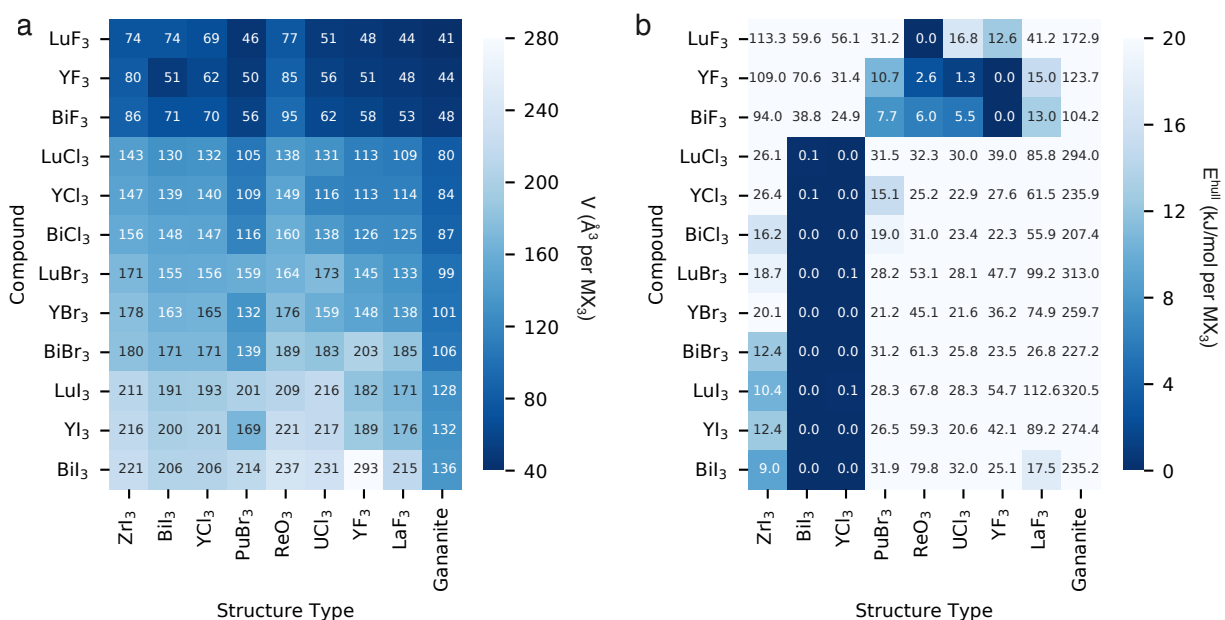

Figure S4: a DFT (PBE) calculated unit cell volumes (V in Å³ per MX₃) per unit formula of MX₃, and **b** DFT calculated formation free energy above convex hull (Eʰᵘˡˡ in kJ mol⁻¹ per MX₃).
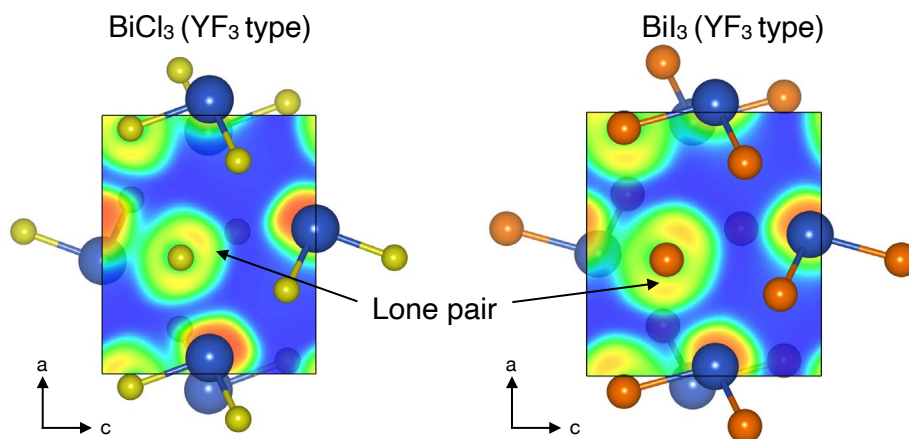
Figure S5: Computed ELFs for **BiCl₃** (left) and **BiI₃** (right) in the **YF₃** type structure. Colour mapping of the ELF vale is shown from 0 (blue) to 1 (red).
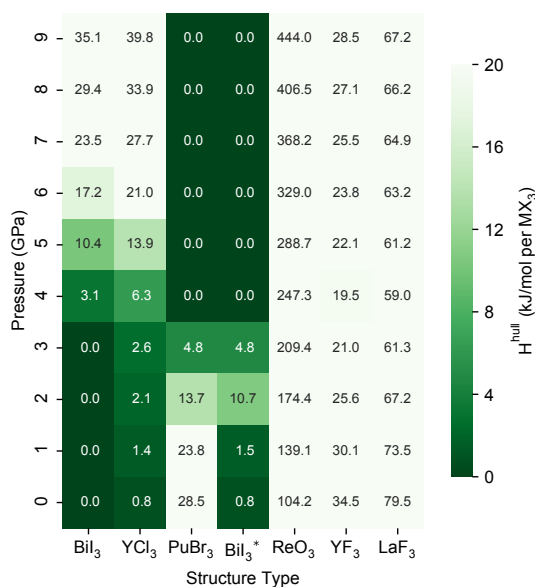

Figure S6: DFT calculated formation enthalpy above convex hull (H^{hull} in kJ mol^{-1}) of **BiI₃** composition in different structure types under pressure. *Experimental high pressure **BiI₃/SbI₃** type as reported by Hsueh et al.[4] which is a distorted **PuBr₃**-type structure with the same dimensionality and coordination number. At low pressure (0∼1 GPa), it transformed back to the layered ambient pressure **YCl₃** type after geometry optimisation.

Effect of Entropy and pV

We computed the free energy of the LuF_3 in both the ReO_3 and the YF_3 structure types. Starting from the fully relaxed PBE+D3 structures, the entropy and zero-point energy (ZPE) corrections were evaluated by computing the frozen-phonon calculations within the harmonic approximation as implemented in the *Phonopy* code.[5] A $3\times3\times3$ and a $2\times2\times2$ supercell was used for ReO_3 and YF_3 types, respectively, and phonons in these supercells were evaluated at the Γ-point.

Table S3: The energy differences between the LuF_3 in the two crystal types, i.e. ReO_3 and YF_3: (1) the DFT total energy (E_{tot}), (2) E_{tot}+zero-point energy (ZPE), and (3) E_{tot}+ZPE+vibrational energy (E_{vib}) at 300 K, respectively.

	E_{tot}	E_{tot}+ZPE (0K)	E_{tot}+ZPE+E_{vib} (300K)
ΔE	7.7	5.3	0.1

As shown in Table S3, the effect of ZPE is ~ 2 kJ/mol per LuF_3, and the total contribution of the vibrational entropy (including ZPE) at 300 K is ~ 7 kJ/mol per LuF_3. We note that the ReO_3 type has the highest volume, i.e. lowest density for all compositions as shown in Figure 2a. Therefore, it is expected that the ReO_3 type will always show the highest values of vibrational entropy. Since the effect of entropy it is still quite small compared with the large E^{hull} of other compositions in the ReO_3 type, especially bromide and iodide-based structures, it is unlikely that other compositions discussed here can form an ReO_3 type framework. The energy contribution of the pV term to the ΔE (ΔG) is negligible, amounting to only 0.002 kJ/mol per LuF_3 at 1 atm. From this analysis, we conclude it is reasonable to use DFT total energies to discuss the relative thermodynamic stability of different polymorphs.

Structure solution of $(H_3O)Yb_3F_{10}\cdot H_2O$

The structure solution based on the powder X-ray diffraction data was conducted by using TOPAS Academic Version 6. After peak searching, the determination of the peak positions and their indexing was performed.The most plausible unit cells and space groups are listed

in the Table below. After Pawley refinements based on these settings, a cubic symmetry of $Fd\bar{3}m$ with a $\sim$ 15.29 Å was selected. Then full structural refinement using the Rietveld method was conducted. The resulting atomic coordinates as well as the bond lengths are listed in Table S5 and S6. The final R-factor were: $R_{bragg} \sim$ 7.71 and $R_{wp} \sim$ 15.07. The structure model is further verified by comparison with the structure of the known Yb analogue $(H_3O)Yb_3F_{10} \cdot H_2O$.

Table S4: List of most possible cell settings from structure solutions.

	Space group	Volume (Å^3)	a (Å)	b (Å)	c (Å)	$\alpha(°)$	$\beta(°)$	$\gamma(°)$
1	$Iba2$	594.475	10.8016	15.2825	3.6013	90	90	90
2	$C2$	468.551	20.1715	15.2816	2.8391	90	147.63	90
3	$F4_132$	3570.464	15.2842	15.2842	15.2842	90	90	90
4	$C2$	405.717	23.0112	10.8127	2.4511	90	138.299	90
5	$I4_1md$	1782.546	10.7999	10.7999	15.2827	90	90	90
6	$Fd\bar{3}m$	3568.08	15.2808	15.2808	15.2808	90	90	90

Table S5: Atomic coordinates of $(H_3O)Yb_3F_{10} \cdot H_2O$, space group $Fd\bar{3}m$ and $a =$ 15.2967(5) Å.

Atoms	x	y	z	Occ.
Lu1	0.375	0.375	0.05182(22)	1
F1	0	0.85652(48)	0.14348(48)	1
F2	0.19173(15)	0.19173(15)	0.19173(15)	1
F3	0.05727(14)	0.05727(14)	0.05727(14)	1
O1	0.5	0.5	0.5	1
O2	0.375	0.375	0.30964(37)	0.3333

Table S6: Bond lengths of $(H_3O)Lu_3F_{10} \cdot H_2O$.

Atom 1	Atom 2	Distance (Å)
Lu1	F1	2.3919
Lu1	F2	2.2220
Lu1	F3	2.2249

References

(1) Larsen, E. M.; Wrazel, J. S.; Hoard, L. G. Single-crystal structures of ZrX_3 (X = Cl^-, Br^-, I^-) and $ZrI_{3.40}$ synthesized in low-temperature aluminum halide melts. *Inorg. Chem.* **1982**, *21*, 2619–2624, DOI: `10.1021/ic00137a018`.

(2) Schleid, T.; Meyer, G.; Morss, L. R. Facile synthesis of UCl_4 and $ThCl_4$, metallothermic reductions of UCl_4 with alkali metals and crystal structure refinements of UCl_3, UCl_4 and Cs_2UCl_6. *J. Less-Common Met.* **1987**, *132*, 69–77, DOI: `10.1016/0022-5088(87)90175-5`.

(3) Hund, F.; Fricke, R. Der Kristallbau von α-BiF_3. *Z. Anorg. Chem.* **1949**, *258*, 198–204, DOI: `10.1002/zaac.19492580310`.

(4) Hsueh, H. C.; Chen, R. K.; Vass, H.; Clark, S. J.; Ackland, G. J.; Poon, W. C.-K.; Crain, J. Compression mechanisms in quasimolecular XI_3 (X=As,Sb,Bi) solids. *Phys. Rev. B* **1998**, *58*, 14812–14822, DOI: `10.1103/physrevb.58.14812`.

(5) Togo, A.; Tanaka, I. First principles phonon calculations in materials science. *Scr. Mater.* **2015**, *108*, 1–5, DOI: `10.1016/j.scriptamat.2015.07.021`.